
Article:

Huang, Jiahui, Fu, Weinong, Niu, Shuangxia et al. (2023) Reduction of Non-working Armature Harmonics in Vernier Permanent Magnet Machines. IEEE Journal of Emerging and Selected Topics in Power Electronics. pp. 6042-6053. ISSN: 2168-6785

https://doi.org/10.1109/JESTPE.2023.3315560

This article has been accepted for publication in IEEE Journal of Emerging and Selected Topics in Power Electronics. This is the author's version which has not been fully edited and content may change prior to final publication. Citation information: DOI 10.1109/JESTPE.2023.3315560

Reduction of Non-Working Armature Harmonics in Vernier Permanent Magnet Machines

Jiahui Huang[1], Weinong Fu[2], Shuangxia Niu[1*], *Senior Member, IEEE,* and Xing Zhao[3], *Member, IEEE*

[1]Department of Electrical Engineering, The Hong Kong Polytechnic University, Hong Kong, eesxniu@polyu.edu.hk
[2]Shenzhen Institutes of Advanced Technology, Chinese Academy of Sciences, Shenzhen 518055, China, wn.fu@siat.ac.cn
[3]Department of Electronic Engineering, University of York, United Kingdom, xing.zhao@york.ac.uk

Abstract—**Vernier permanent magnet machines (VPMM) are becoming increasingly attractive for low-speed direct drive industrial applications. This paper presents a novel design perspective of reducing non-working even-order armature harmonics in VPMMs with concentrated winding to further improve the overall electromagnetic performance. The armature reaction MMF harmonics can be adjusted by controlling the winding layout. In particular, a dual-stator VPMM (DS-VPMM) is presented, in which the inner stator is shifted by a half slot pitch relative to the outer stator, and the key is that dual concentrated windings are reversely connected in series with a 180-degree mechanical angle difference. Consequently, those non-working even-order harmonics produced by the armature reaction can be eliminated. As a result, the synchronous inductance is notably reduced, which further improves the power factor without sacrificing torque density. A non-dominated sorting genetic algorithm II (NSGA-II) is adopted in the optimization process to obtain optimal parameters of the proposed design. The finite-element analysis (FEA) results show that, compared to conventional VPMMs, the proposed design with reduced even-order armature harmonics exhibits higher torque density and higher power factor while the unbalanced force is mitigated. Finally, a prototype is fabricated to verify this proposed approach.**

Index Terms—**Armature reaction, concentrated winding, even-order harmonics, split-tooth, Vernier machine.**

I. INTRODUCTION

PERMANENT magnet (PM) machines have been extensively studied and widely adopted in various practical applications due to their high efficiency, torque density, and reliability [1]-[3]. With the development of flux modulation PM machines, Vernier machines have emerged as competitive candidates for low-speed direct-drive applications in electrified transportation owing to their higher torque density compared to conventional permanent magnet (PM) machines [4]-[6]. A number of studies have explored novel structures to further improve torque density, including dual-stator, dual-sided PM, claw-pole, coding-shaped tooth, etc.[7]-[11]. However, the utilization of the flux modulation effect in Vernier machines brings a high torque density but simultaneously leads to a low power factor [12]. The characteristic of low power factor has become a major problem in Vernier machines, which requires converters with larger capacity for the same output power. Taking into consideration of the driving system, this issue severely limits the application potential of conventional Vernier machines.

Therefore, the issue of the low power factor has received considerable attention, and several attempts have been made to address this issue [13]-[17]. Generally, the enhancement of the air gap flux density and reduction of the inductance are the two possible ways to improve the power factor. A high power factor Halbach-type Vernier machine without a rotor iron core was proposed in [13]. In that design, an elevated back electromotive force (EMF) and a reduced synchronous inductance facilitate the improvement of the power factor. However, compared with typical machines with an iron core structure, the output torque is severely reduced. Meanwhile, the auxiliary DC field winding is used to improve the power factor in [14], [15]. The DC winding provides an additional excitation to enhance the air gap flux density, but it leads to more copper loss at the same time. Furthermore, dual-stator Vernier machines with higher power factors were proposed in [16], [17]. In [16], a complementary arrangement of dual stators is utilized to reduce the flux leakage and enhance the air gap flux density. As a result, the machine exhibits a high power factor of 0.9, which is significantly improved compared with a conventional surface-mounted PM Vernier machine. At the same time, literature [17] well studied the mechanism for the power factor enhancement due to the dual stator topology, which reveals the underlying reason for improving modulated air gap flux density.

The aforementioned methods are mainly focused on the air gap flux density improvement as well as the back EMF. According to [18]-[21], reducing the non-working armature reaction MMF harmonics for the decrease of the inductance is another appealing option. As illustrated in [22], several techniques have been investigated to reduce the harmonics, including adding magnetic flux barriers in stator yoke [23], [24], using the coils with different turns [25], applying multilayer fractional-slot concentrated winding (FSCW) [26], adopting multiphase FSCW [27], using dual slot layer stator [28], etc. However, the first four methods listed above can only reduce the low-order harmonics. The dual slot layer stator [28] can simultaneously reduce the low-order and high-order harmonics, but the issue of fundamental harmonic reduction (~37%) cannot be ignored. Hence, the armature winding with coil pitch of two slot pitches proposed in [29], [30] is a competitive method to reduce the harmonics in conventional PM machines, which eliminates the low-order and high-order harmonics simultaneously while the fundamental harmonic is not affected. In [18], this promising winding structure was applied and well-studied in Vernier machines to achieve a higher power factor, and the design guideline based on the theoretical analysis was also proposed. Additionally, a hybrid concentrated-winding (CW) achieved through delta and star winding connection was also investigated in a Vernier machine to reduce sub- and high-order harmonics, effectively improving the power factor[21].

This paper presents a novel dual-stator Vernier permanent magnet machine (DS-VPMM) with a special armature winding arrangement in which the two sets of windings in the inner and outer stator are reversely connected in series and arranged in a 180-degree mechanical angle difference. Instead of only focusing on one method to improve the power factor, the proposed machine combines the advantages of a dual-stator structure and an advanced winding design. Consequently, a high power factor and improved torque density can be both achieved due to the reduced non-working harmonics and enhanced air gap flux density. The proposed structure and working principle are described in Section II. Then, in Section III, a non-dominated sorting genetic algorithm II (NSGAII) is adopted to conduct the global optimization of the proposed machine. To showcase the superiorities of the proposed design, Section IV compares the electromagnetic performance between the proposed DS-VPMM and the conventional Vernier machine. To validate the performance prediction, a prototype is manufactured and tested in Section V.

II. MACHINE STRUCTURE AND WORKING PRINCIPLE

A. Origination of the Proposed Structure

The power factor can be improved by either reducing the inductance or enhancing the back EMF. Based on this design concept, a novel DS-VPMM comprised of two split-tooth stators and a sandwiched rotor constituted with PMs is proposed, as shown in Fig. 1, and the main design parameters are listed in Table I.

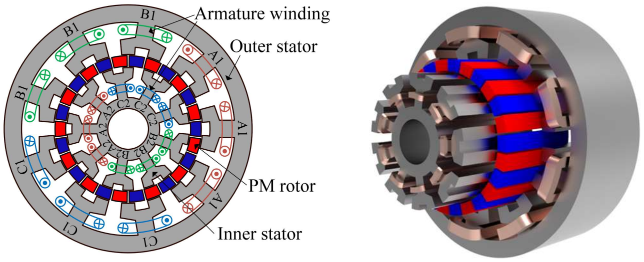

Fig. 1. The structure of the proposed DS-VPMM.

TABLE I
MAIN DESIGN PARAMETERS OF THE PROPOSED MACHINE

Parameters	Value
Number of stator slots	9
Number of rotor pole pairs	13
Stator outer diameter (mm)	200
Stack length (mm)	75
Air gap length (mm)	1
Rated speed (rpm)	300
PM material	N38EH
Steel material	WG35WW300

Different from the conventional split-tooth Vernier machine, the split teeth in both inner and outer stators serve as the flux modulator. Meanwhile, the armature winding structure is innovatively arranged. As shown in Fig. 2, the armature winding employs a double-layer concentrated connection. The integrated armature winding consists of two sets of windings, including outer stator winding (winding 1) and inner stator winding (winding 2). The windings on both stators are connected in series, and the inner stator winding is shifted by 180-mechanical-degree with an inverse connection compared with the armature winding on the outer stator. By adopting this novel winding topology, the non-working even-order space harmonics can be effectively reduced, and the synchronous inductance can be reduced at the same time, which will be expanded in detail in the next part. Hence, the proposed machine can achieve a higher power factor and enhanced torque density.

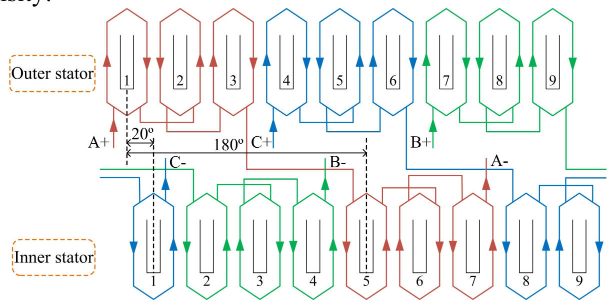

Fig. 2. The proposed inner and outer winding connection.

B. Working Harmonics Analysis

Similar to conventional Vernier machines, the working principle of the proposed machine is based on the flux modulation effect [31]. However, compared with the conventional design, the magnetic field produced by the rotor PMs in the proposed machine is modulated by both inner and outer stator teeth simultaneously. Consequently, abundant air gap field harmonics are generated and contribute to torque production. In this part, a magnetomotive force (MMF)-permeance analytical model is adopted to identify the working harmonics of the proposed machine.

The MMF produced by rotor PMs can be simplified as a square waveform and expressed in Fourier series expansion as

$$F_{pmr}(\theta,t)=\sum_{n=1}^{+\infty}F_n\cos[nN_r(\theta-\Omega_r t)] \tag{1}$$

where F_n denotes the magnitudes of PM MMF harmonics, θ is the circumferential position in the air gap, Ω_r is the mechanical angular speed of the rotor, N_r is the number of the PM pole pairs, and n is the order of the Fourier series.

The air gap permeance due to both inner and outer stators can be obtained by

$$\Lambda_s(\theta)=\frac{\Lambda_{s1}(\theta)\cdot\Lambda_{s2}(\theta)}{\frac{\mu_0}{g}} \tag{2}$$

where $\Lambda_{s1}(\theta)$ is the outer stator permeance, $\Lambda_{s2}(\theta)$ is the inner stator permeance, μ_0 is the permeability of the vacuum, and g denotes the air gap length. Using Fourier expansion, the permeance functions of both stators are given in (3) and (4)

$$\Lambda_{s1}(\theta)=\Lambda_0+\sum_{k=1}^{+\infty}\Lambda_k\cos(kN_s\theta) \tag{3}$$

$$\Lambda_{s2}(\theta)=\Lambda'_0+\sum_{k=1}^{+\infty}\Lambda'_k\cos(kN_s\theta+\theta_0) \tag{4}$$

where Λ_0 and Λ'_0 are the average values of the outer and inner stator permeance, respectively. Λ_k and Λ'_k refer to the amplitude of the k^{th} harmonic of the outer and inner stator, respectively. N_s represents the number of flux modulators which equals the product of the number of stator slots (N_{slot}) and the number of flux modulators per stator tooth (N_m) as presented in (5). θ_0 is the mechanical angle difference between the inner and outer stators, which is shown in (6)

$$N_s = N_{slot} N_m \tag{5}$$

$$\theta_0 = \frac{2\pi}{N_s} = \frac{\pi}{9} \tag{6}$$

Therefore, the equivalent air gap permeance $\Lambda_s(\theta)$ can be obtained by combining (2)-(6)

$$\begin{aligned}\Lambda_s(\theta) = \frac{g}{\mu_0}\{&\Lambda_0\Lambda'_0 + \Lambda_0\sum_{k=1}^{+\infty}\Lambda'_k\cos(kN_s\theta+\theta_0)\\ &+\Lambda'_0\sum_{k=1}^{+\infty}\Lambda_k\cos(kN_s\theta) + \sum_{k=1}^{+\infty}\frac{\Lambda_k\Lambda'_k}{2}\cos[(2kN_s\theta)+\cos\theta_0]\}\end{aligned} \tag{7}$$

Hence, the air gap flux can be derived by the product of (1) and (7)

$$\begin{aligned}&B_g(\theta,t) = F_{pmr}(\theta,t)\Lambda_s(\theta)\\ &= \frac{g}{\mu_0}\sum_{n=1}^{+\infty}\sum_{k=1}^{+\infty}(\Lambda_0\Lambda'_0 + \frac{\Lambda_k\Lambda'_k}{2}\cos\frac{\pi}{9})F_n\cos[nN_r(\theta-\Omega_r t)]\\ &+\frac{g}{\mu_0}\sum_{n=1}^{+\infty}\sum_{k=1}^{+\infty}\frac{\Lambda_0 F_n\Lambda'_k}{2}\cos[(kN_s \pm nN_r)\theta \mp nN_r\Omega_r t + \frac{\pi}{9}]\\ &+\frac{g}{\mu_0}\sum_{n=1}^{+\infty}\sum_{k=1}^{+\infty}\frac{\Lambda'_0 F_n\Lambda_k}{2}\cos[(kN_s \pm nN_r)\theta \mp nN_r\Omega_r t]\\ &+\frac{g}{\mu_0}\sum_{n=1}^{+\infty}\sum_{k=1}^{+\infty}\frac{F_n\Lambda_k\Lambda'_k}{4}\{\cos[(2kN_s \pm nN_r)\theta \mp nN_r\Omega_r t]\end{aligned} \tag{8}$$

Based on (8), the air-gap flux density harmonics produced by rotor PMs are summarized in Table II. The harmonics can be divided into five groups. The harmonics with orders of nN_r in Group I are the original PM harmonics without modulation. Besides, the harmonics in Groups II, III, IV, and V are the harmonics after modulation. The positive and negative speed of the modulated harmonics represents the consistency compared with the rotor rotating direction. In the proposed machine, N_r equals 13, and the n=1,3,5…etc. The space harmonic orders in all five groups are in odd numbers.

TABLE II
HARMONICS OF AIR GAP FLUX DENSITY EXCITED BY ROTOR PMS

Group number	Space harmonic order	Rotating speed
I	nN_r	Ω_r
II	$kN_s + nN_r$	$\frac{nN_r}{kN_s + nN_r}\Omega_r$
III	$kN_s - nN_r$	$-\frac{nN_r}{kN_s - nN_r}\Omega_r$
IV	$2kN_s + nN_r$	$\frac{nN_r}{2kN_s + nN_r}\Omega_r$
V	$2kN_s - nN_r$	$-\frac{nN_r}{2kN_s - nN_r}\Omega_r$

C. Inductance Analysis

Fig. 3 shows the phasor diagram when the I_d =0 control strategy is applied and the stator resistance is ignored. Consequently, the power factor can be derived from Fig. 3, which is given as follows.

$$\cos\varphi = \frac{1}{\sqrt{1+\left(\frac{X_s I_s}{E_0}\right)^2}} = \frac{1}{\sqrt{1+\left(\frac{\omega_e L_s I_s}{E_0}\right)^2}} \tag{9}$$

where I_s is the stator current, ω_e is the electrical angular speed, X_s is the synchronous reactance, L_s is the synchronous inductance, and E_0 represents the back EMF.

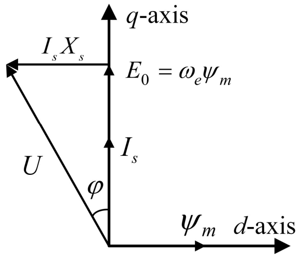

Fig. 3. Phasor diagram of Vernier machines.

According to the flux modulation theory [31], the pole-pair number of the armature winding is given as follows.

$$P_a = N_s - N_r \tag{10}$$

In the conventional FSCW design, a lot of space harmonics are produced in the air gap, including several undesired non-working space harmonics. These non-working harmonics lead to an unexpected increase in inductance. It is obvious from (9) that reducing the inductance is a very effective method to improve the power factor when the electrical angular speed and back EMF are kept constant. Hence, in this paper, a novel winding arrangement is proposed to eliminate the even-order space harmonics of armature reaction MMF, which further reduces the inductance. Meanwhile, the odd-order working harmonics are unaffected.

The mechanism of the inductance reduction is illustrated as follows. The synchronous inductance can be expressed as

$$L_s = L_{ms} + L_{lk} \tag{11}$$

where L_{ms} is the inductance of the armature reaction, and L_{lk} is the leakage inductance.

The L_{ms} can be obtained by

$$L_{ms} = \frac{\psi_a}{I_m} \tag{12}$$

$$\psi_a = r_g l_{ef}\int_0^{2\pi} B_w(\theta,t)N_a(\theta)d\theta \tag{13}$$

where ψ_a is the flux linkage of phase A, I_m is the peak value of the phase current, r_g is the air gap radius, l_{ef} is the effective length of the machine, B_w is the flux density produced by armature winding, and N_a is the winding function of phase A as given in (14) [32]

$$N_a(\theta) = \sum_{v=1}\frac{2N_t k_{wv}}{v\pi}\cos(v\theta) \tag{14}$$

where N_t is the total number of turns in phase A, v is the winding harmonics, and k_{wv} is the winding factor of the v^{th} harmonic.

The armature reaction MMF of the proposed winding and the corresponding air gap flux density are given in Fig. 4. The MMF of three-phase armature winding is expressed as

$$F_{aw} = i_a(t)N_a(\theta) + i_b(t)N_b(\theta) + i_c(t)N_c(\theta) \tag{15}$$

This article has been accepted for publication in IEEE Journal of Emerging and Selected Topics in Power Electronics. This is the author's version which has not been fully edited and content may change prior to final publication. Citation information: DOI 10.1109/JESTPE.2023.3315560

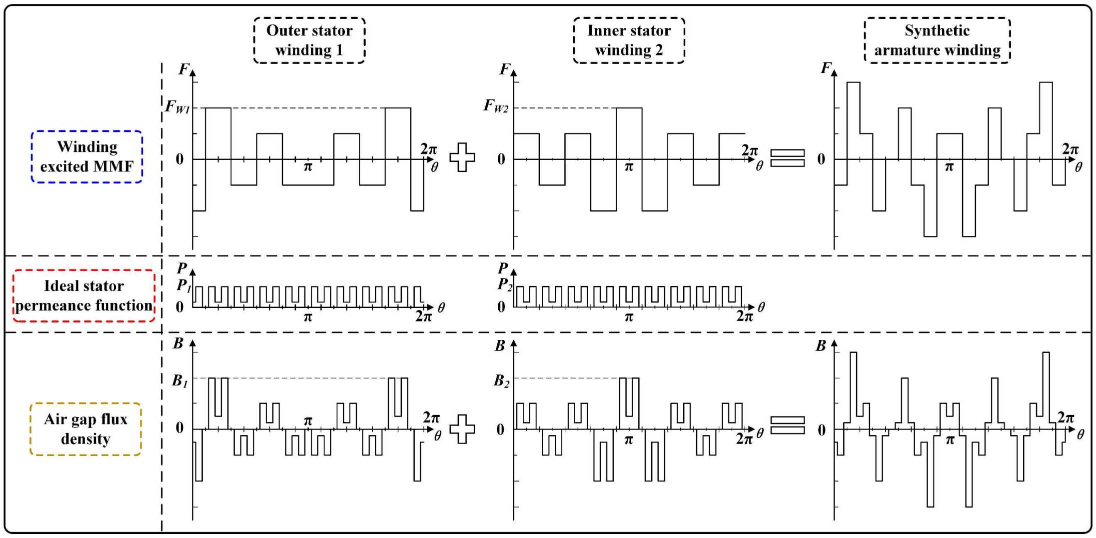

Fig. 4. Armature winding MMF and air gap flux density waveforms.

where i_a, i_b, and i_c are the current of phases A, B, and C, respectively.

In the proposed machine, the armature winding is split into winding 1 and winding 2, respectively, which are connected in series. To eliminate the even-order harmonics, the polarity of winding 2 is inversed, and the position is shifted by 180-degree (δ) compared to winding1. The MMFs of both winding sets are expressed separately in (16) and (17). Their corresponding MMF waveforms are depicted in Fig.4, which agree well with the winding arrangement. The MMF waveform of winding 2 is inversed and shifted 180 degrees compared to winding 1. The MMFs of winding 1 and winding 2 are given as follows

$$F_{aw1}=\frac{3}{2}\sum_{\substack{v=3k\pm1\\k=0,1,2...}}\frac{2\frac{N_t}{2}k_{wv}}{v\pi}I_m\cos(wt-v\theta) \tag{16}$$

$$F_{aw2}=\frac{3}{2}\sum_{\substack{v=3k\pm1\\k=0,1,2...}}\frac{2\frac{N_t}{2}k_{wv}}{v\pi}[-I_m\cos(wt-v(\theta-\delta))] \tag{17}$$

Consequently, the synthetic MMF can be obtained by superposition of the MMF of winding 1 and winding 2, which is expressed as follows.

$$F_{aw}=F_{aw1}+F_{aw2} \tag{18}$$

$$\begin{cases}F_{aw}=\dfrac{3}{2}\dfrac{2N_tk_{wv}}{v\pi}I_m\cos(wt-v\theta), & v \text{ is } odd\\ F_{aw}=0 & , v \text{ is } even\end{cases} \tag{19}$$

$$F_{aw}=\frac{3}{2}\sum_{\substack{v=6k\pm1\\k=0,1,2...}}\frac{2N_tk_{wv}}{v\pi}I_m\cos(wt-v\theta) \tag{20}$$

It can be observed that only the odd-order harmonics exist from the above equations. The waveform of synthetic MMF in Fig. 4 also shows the elimination of the even-order harmonics.

Considering the modulation effect of the split teeth, the air gap flux density excited by an individual winding set and the resultant air gap flux density are illustrated in the lower position of Fig. 4, which exhibits a similar even-order harmonic elimination effect.

To validate the aforementioned analysis, the air gap flux density waveforms excited by armature windings obtained through finite element analysis (FEA) are presented in Fig. 5 and Fig.6. The waveforms of air gap flux densities excited by outer stator winding and inner stator winding are depicted in Fig. 5(a) and (b), respectively. It can be observed that the simulation results are consistent with the waveforms presented in Fig. 4. In addition, Fig. 6 presents the synthetic air gap flux density excited by both sets of armature windings. The fast Fourier transform (FFT) results in Fig. 6 (b) show that only odd-order harmonics exist, thereby validating the foregoing analysis.

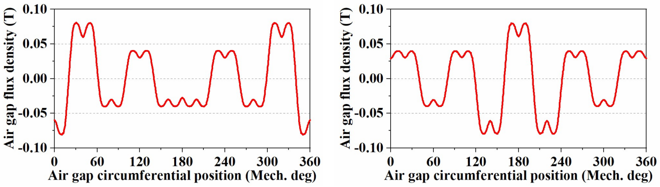

(a) (b)

Fig. 5. Air gap flux densities excited by a single set of armature winding. (a) Outer stator winding. (b) Inner stator winding.

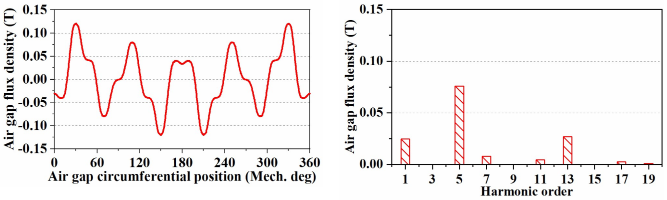

(a) (b)

Fig. 6. Air gap flux density excited by both sets of the armature windings. (a) Waveform. (b) Harmonic distribution.

Accordingly, the resultant flux density can be expressed as

$$B_w(\theta,t)=F_{\mathrm{aw}}\cdot\Lambda_s(\theta) \tag{21}$$

Therefore, the flux linkage and inductance in phase A can be deduced.

$$\psi_a\approx\frac{3}{2}\pi\frac{g}{\mu_0}\Lambda_0\Lambda'_0I_mr_gl_{ef}\sum_{\substack{v=6k\pm1\\k=0,1,2...}}[\left(\frac{2N_tk_{wv}}{v\pi}\right)^2\cos(wt)] \tag{22}$$

$$L_{ms}=\frac{\psi_a}{\mathrm{I}_m}=\frac{3}{2}\pi\frac{g}{\mu_0}\Lambda_0\Lambda'_0r_gl_{ef}\sum_{\substack{v=6k\pm1\\k=0,1,2...}}\left(\frac{2N_tk_{wv}}{v\pi}\right)^2 \tag{23}$$

This article has been accepted for publication in IEEE Journal of Emerging and Selected Topics in Power Electronics. This is the author's version which has not been fully edited and content may change prior to final publication. Citation information: DOI 10.1109/JESTPE.2023.3315560

According to (23), v=6k±1 in the proposed machine is different from v=3k±1 in the conventional design. Obviously, only odd-order harmonics exist in the proposed design, while the conventional design contains both even-order and odd-order harmonics. Therefore, the inductance in the proposed machine is reduced, and the power factor is improved compared to the conventional split-tooth Vernier machine.

III. DESIGN OPTIMIZATION

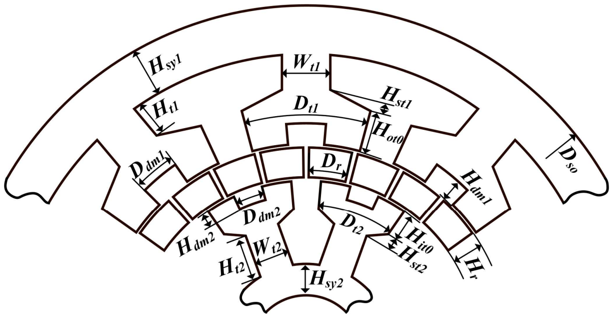

Fig. 7. Main structural parameters of the proposed DS-VPMM.

The proposed machine has a large number of structural design parameters, as shown in Fig. 7. In order to obtain the optimal values of these parameters, the NSGA II is adopted for design optimization. Maximizing average torque and power factor are the objectives of this optimization, which can be expressed as

$$max\begin{cases} f_1(x), & f_1(x)=T_{avg} \\ f_2(x), & f_2(x)=P_f \end{cases} \tag{24}$$

where T_{avg} is the average output torque, and P_f refers to the power factor. Among all parameters, the outer diameter, the stack length of the iron core, and the air gap length are fixed, and the other 18 design parameters can vary in certain ranges, as listed in Table III. Meanwhile, the constraints are listed as

$$\begin{cases} J=5A/mm^2 \\ P_f \geq 0.5 \end{cases} \tag{25}$$

where J is the current density.

TABLE III
DESIGN PARAMETERS AND THE VARIATION RANGES

Parameters	Range
Height of outer stator yoke (H_{sy1})	5-15 mm
Height of outer stator main tooth (H_{t1})	5-15 mm
Height between outer stator main tooth and split tooth (H_{st1})	0.5-5 mm
Height of outer stator split tooth (H_{ot0})	3-10 mm
Width of outer stator main tooth (W_{t1})	10-28 mm
Arc of one outer stator split teeth unit (D_{t1})	20-35 deg
Arc of outer stator dummy slot (D_{dm1})	2-15 deg
Height of outer stator dummy slot (H_{dm1})	1-8 mm
Height of rotor PM (H_r)	3-12 mm
Arc of rotor PM (D_r)	9-13.2 deg
Height of inner stator yoke (H_{sy2})	8-15 mm
Height of inner stator main tooth (H_{t2})	8-20 mm
Height between inner stator main tooth and split tooth (H_{st2})	0.5-5 mm
Height of inner stator split tooth (H_{it0})	3-10 mm
Width of inner stator main tooth (W_{t2})	5-15 mm
Arc of one inner stator split teeth unit (D_{t2})	20-35 deg
Arc of inner stator dummy slot (D_{dm2})	2-15 deg
Height of inner stator dummy slot (H_{dm2})	1-8 mm

The optimization process is illustrated in Fig.8. In this optimization process, the FEA program is embedded into NSGA-II for the computation of the machine performance. Firstly, the models with different values of the design parameters in the 1st generation are generated and calculated. Then, the results are saved and ranked based on the objectives. Secondly, the child population is generated by mutation and crossover, which is calculated as follows. The parent and child individuals are combined, and 100 individuals are selected based on the ranking result. Finally, the optimization progress is finished if the generation reaches the maximum number. The generation number during optimization is 50, and the population number in each generation is 100. Moreover, the crossover and mutation factors are chosen as 0.8 and 0.05, respectively.

The optimization result, which shows the tradeoff between the average torque and power factor, is shown in Fig. 9. The Pareto front curve of this scatter diagram is marked with a black line. In addition, a turning point located on the Pareto front curve is selected as the optimal design and highlighted by the red circle, which has both relatively high average torque and power factor.

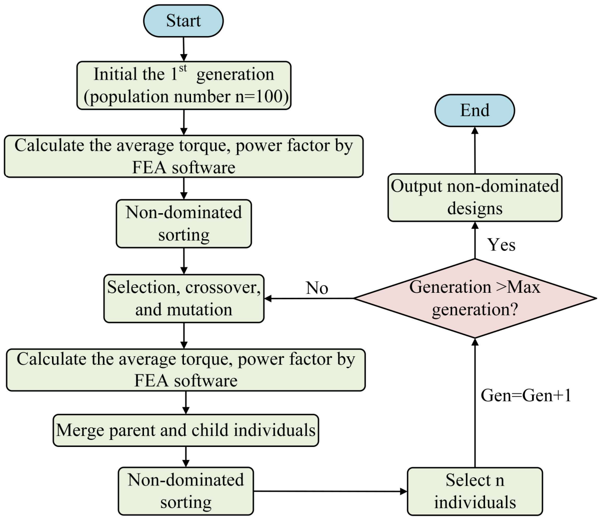

Fig.8. Flow chart of the optimization process.

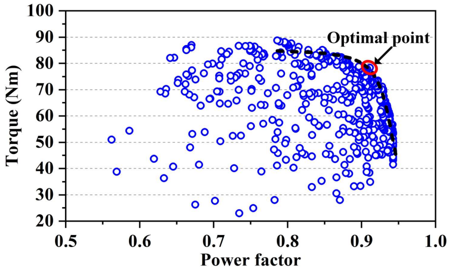

Fig.9. Optimization result of the proposed DS-VPMM.

IV. ELECTROMAGNETIC PERFORMANCE COMPARISON

To demonstrate the merits of the proposed DS-VPMM, a performance comparison is conducted between the proposed machine and the conventional multi-tooth Vernier machine. To perform a fair comparison, the conventional machine is also

This article has been accepted for publication in IEEE Journal of Emerging and Selected Topics in Power Electronics. This is the author's version which has not been fully edited and content may change prior to final publication. Citation information: DOI 10.1109/JESTPE.2023.3315560

globally optimized under the same overall size and air gap length as the proposed machine. The optimized design parameters of both machines are listed in Table IV.

TABLE IV
THE OPTIMIZED DESIGN PARAMETERS

Parameters	Conventional machine	Proposed machine
Stator outer diameter	200 mm	
Stack length of iron core	75 mm	
Air gap length	1 mm	
Current density	5 A/mm^2	
Phase number of turns in series	420	
Rated speed	300 rpm	
Height of outer stator yoke (H_{sy1})	10.1 mm	8.1 mm
Height of outer stator main tooth (H_{t1})	16.8 mm	8.8 mm
Height between outer stator main tooth and split tooth (H_{st1})	3.5 mm	2.2 mm
Height of outer stator split tooth (H_{ot0})	4.9 mm	3.5 mm
Width of outer stator main tooth (W_{t1})	17.4 mm	23.9 mm
Arc of one outer stator split teeth unit (D_{t1})	33 deg	31 deg
Arc of outer stator dummy slot (D_{dm1})	15.5 deg	9 deg
Height of outer stator dummy slot (H_{dm1})	3.5 mm	4.6 mm
Height of rotor PM (H_r)	7.5 mm	10 mm
Height of rotor yoke (H_{yr})	14 mm	/
Arc of rotor PM (D_r)	12.35 deg	12.5 deg
Height of inner stator yoke (H_{sy2})	/	11.9 mm
Height of inner stator main tooth (H_{t2})	/	18.1 mm
Height between inner stator main tooth and split tooth (H_{st2})	/	2.6 mm
Height of inner stator split tooth (H_{it0})	/	4.9 mm
Width of inner stator main tooth (W_{t2})	/	13.4 mm
Arc of one inner stator split teeth unit (D_{t2})	/	31 deg
Arc of inner stator dummy slot (D_{dm2})	/	9 deg
Height of inner stator dummy slot (H_{dm2})	/	2.5 mm

A. Open-Circuit Performances

Fig. 10 shows the optimal structures of both machines and the corresponding open-circuit magnetic field distribution. Obviously, a modulation field with five pole pairs can be found in both machines. The no-load air gap flux density waveforms and the spectrums of both machines are shown in Fig. 11, which further validates the existence of the five pole pairs component. It can be observed that, apart from the fundamental harmonic of 13 pole pairs, several odd-order harmonics also exist due to the modulation effect and contribute to the torque production, which matches well with the analysis in Section II.

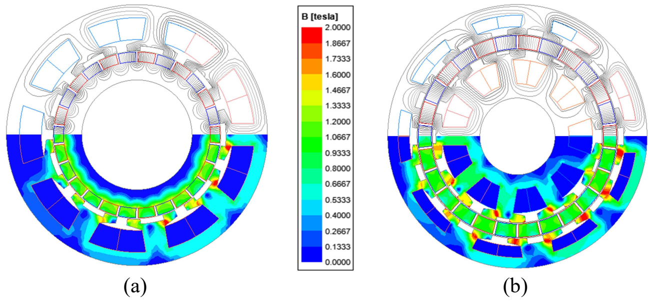

(a) (b)

Fig. 10. Open-circuit magnetic field distribution. (a) Conventional machine. (b) Proposed DS-VPMM.

The no-load phase back EMF waveforms and spectra of the proposed and conventional machines at 300 rpm are compared in Fig. 12. Apparently, the back EMF waveforms of both machines are sinusoidal, while the proposed machine has a higher amplitude. As shown in Fig. 12 (b), the proposed machine has a larger fundamental component. Meanwhile, the third-order harmonic is also increased in the proposed machine. However, it can be ignored since it can be eliminated in the line back EMF waveform in a three-phase machine.

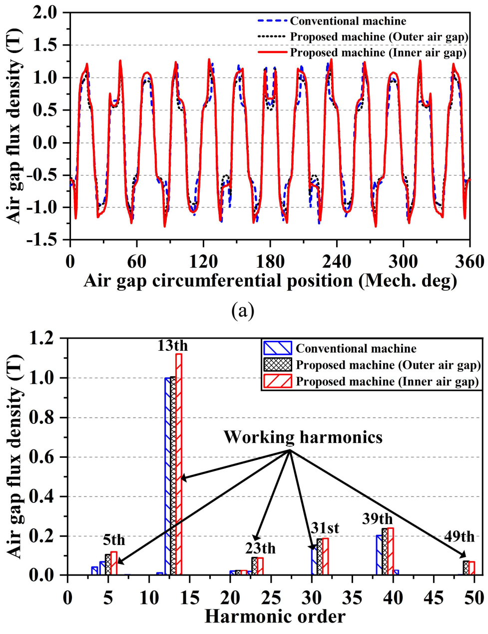

(a)

(b)

Fig. 11. Open-circuit air gap flux density. (a) Waveforms. (b) Harmonics.

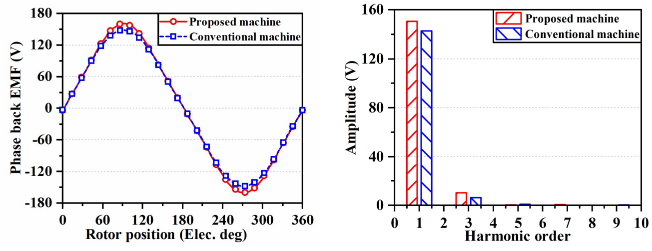

(a) (b)

Fig. 12. No-load back EMF. (a) Waveforms. (b) Harmonics distribution.

B. On-load Performance

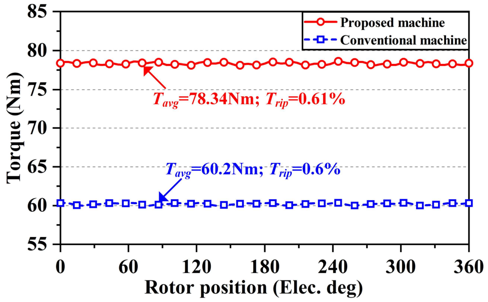

Fig. 13. Torque performance comparison.

Fig. 13 shows the torque comparison between the conventional machine and the proposed DS-VPMM under the rated condition (current density=5 A/mm^2). Both machines have a relatively low torque ripple of lower than 1%. Meanwhile, the proposed machine exhibits a 30.1% larger average torque than the conventional machine, which is mainly attributed to the enhanced air-gap flux density working harmonics.

This article has been accepted for publication in IEEE Journal of Emerging and Selected Topics in Power Electronics. This is the author's version which has not been fully edited and content may change prior to final publication. Citation information: DOI 10.1109/JESTPE.2023.3315560

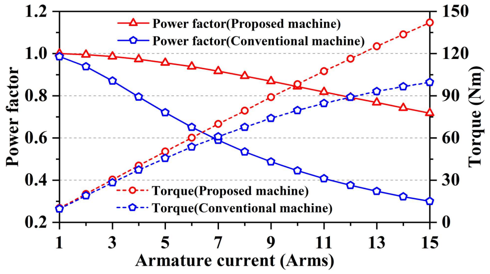

Fig. 14. Torque and power factor versus the input current.

Fig. 14 compares the torque and power factor of both machines under different input currents. The proposed machine demonstrates a better overload capacity compared with the conventional machine. It can be found that there is no clear difference in average torque and power factor between the conventional machine and the proposed machine when the current is very low. However, with increasing currents, the proposed machine has a much larger output torque and power factor than the conventional machine. The proposed machine performs better linearity in torque performance under overload conditions. Meanwhile, with the current increasing from 1A to 15A, the proposed machine experiences a decrease in power factor to approximately 0.72, which is significantly less drastic than the sharp drop to 0.3 of the conventional machine.

The excellent overload capability of the proposed machine is mainly due to the reduced armature reaction. The non-working harmonics of the armature winding are notably reduced, while the working harmonics are unaffected. Fig. 15 compares the flux density distribution of the conventional and proposed machines under an overload condition with a current of 15 A. The conventional machine performs more serious saturation, which increases the magnetic reluctance and reduces the effective magnetic loading. Hence, the torque production of the conventional machine under the overload condition is affected, which drops sharply with the increase of currents compared to the proposed machine.

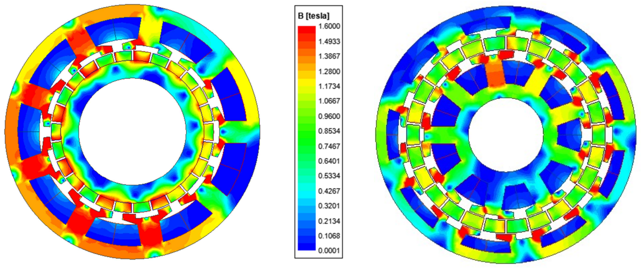

(a) (b)

Fig. 15. Flux density distribution of both machines under an overload condition. (a) Conventional machine. (b) Proposed DS-VPMM.

The reduced armature reaction MMF harmonics are also reflected in a smaller inductance, as shown in Fig. 16. Fig.16 presents the synchronous inductance of both machines. Compared with the conventional machine, the inductance of the proposed machine is reduced a lot, which is only 36.4% of the conventional machine. The result well validates the theoretical analysis in Section II. In addition, the smaller inductance also contributes to the improved power factor, as illustrated in (1). Fig. 17 depicts the induced voltages with only the fundamental harmonics of both machines under the 7A input current. The power factor angles of both machines can be easily obtained for calculating the corresponding power factors. Obviously, the proposed machine has a much smaller power factor angle, which results in a higher power factor.

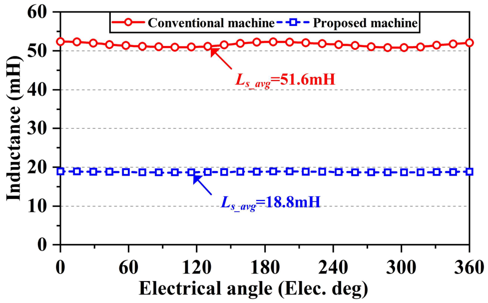

Fig. 16. Comparison of synchronous inductance.

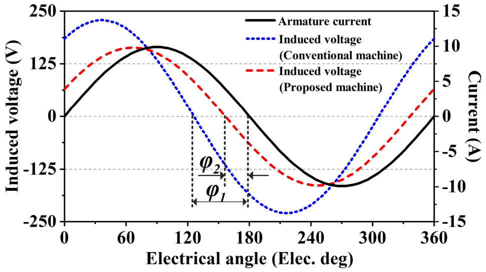

Fig. 17. Input current and induced voltage. (Current=7A, 300rpm)

C. Radial Unbalanced Magnetic Force

The radial unbalanced magnetic force is a non-neglectable issue in industrial applications. The dual-stator machines typically perform lower unbalanced forces compared to conventional single-stator machines due to a more symmetrical magnetic field distribution. Fig. 18 (a) and (b) illustrate the open-circuit field distributions of both conventional and proposed machines, respectively. It is evident that the flux distribution of the proposed DS-VPMM is more symmetrical than that of the conventional machine. Consequently, the unbalanced force of the proposed machine under no-load conditions is significantly reduced compared to the conventional machine, with a reduction of approximately 74.65%, as shown in Fig. 19(a).

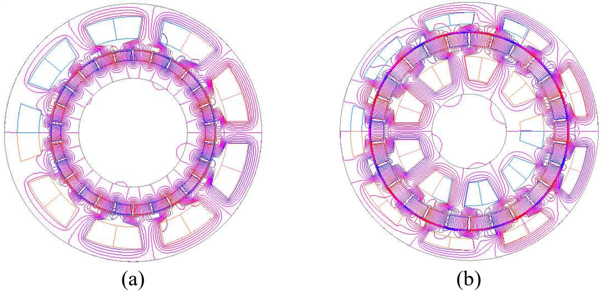

(a) (b)

Fig. 18. Open-circuit magnetic field distribution of both machines. (a) Conventional machine. (b) Proposed DS-VPMM.

Fig. 19 (a) and Fig. 19(b) compare the unbalanced force between the conventional machine and the proposed machine under no-load and the rated conditions, respectively. It is clear that, in both machines, the unbalanced force is much higher under the rated condition. This is mainly due to the influence of the armature reaction field. Fig. 20 shows the armature reaction field distributions of both machines. In the proposed machine, an additional set of the inner stator winding is reversed and arranged in a 180 mechanical degree difference from the outer

This article has been accepted for publication in IEEE Journal of Emerging and Selected Topics in Power Electronics. This is the author's version which has not been fully edited and content may change prior to final publication. Citation information: DOI 10.1109/JESTPE.2023.3315560

stator winding, effectively resolving the asymmetrical displacement issue of phase windings observed in the conventional machine. Consequently, the proposed machine exhibits a more uniform flux distribution across the entire structure compared to the conventional machine. Thus, due to the compensation effect of the inner stator and winding, the unbalanced force of the proposed DS-VPMM under the rated condition is significantly reduced compared to the conventional machine as well. Specifically, the unbalanced force is 76.4% lower than that of the conventional machine, as shown in Fig. 19 (b).

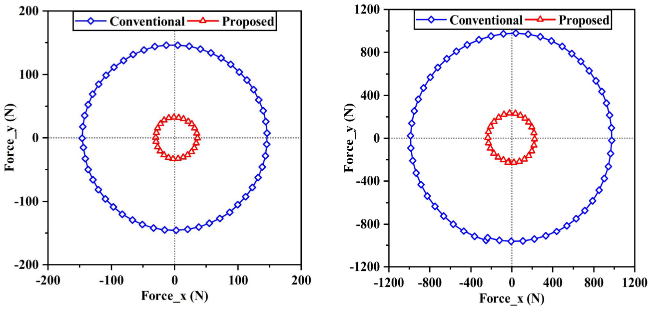

(a) (b)

Fig. 19. Radial unbalanced magnetic force. (a) No-load condition. (b) Rated condition.

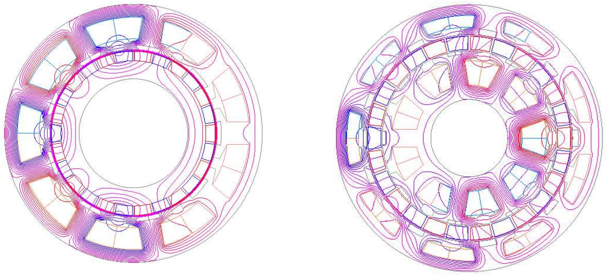

(a) (b)

Fig. 20. Armature reaction field distribution of both machines. (a) Conventional machine. (b) Proposed DS-VPMM.

D. Loss and Efficiency

The detailed electromagnetic performance comparison is summarized in Table V. The main losses, including copper loss, core loss, and PM eddy current loss, are well investigated. It can be found that the average torque of the proposed machine is improved. However, compared with the conventional machine, the main losses of the proposed machine are increased as well. Consequently, the overall efficiency increases from 89.9% to 91.1%.

TABLE V
PERFORMANCE COMPARISON OF THE CONVENTIONAL AND PROPOSED VERNIER MACHINES

Items	Conventional machine	Proposed machine
Torque (Nm)	60.2	78.34
Cogging torque (Nm)	0.115	0.31
Torque ripple (%)	0.6	0.61
Synchronous inductance (mH)	51.6	18.8
Power factor	0.62	0.91
Unbalanced force (N)	988	233
Copper loss (W)	196	209
Core loss (W)	11.1	16.2
PM eddy current loss (W)	5.8	15
Efficiency	89.9%	91.1%

V. PROTOTYPE FABRICATION AND EXPERIMENTAL VALIDATION

To verify the foregoing analysis, a prototype is manufactured and tested. The relevant dimensions are listed in Table IV, and the mechanical structure design is shown in Fig. 21. As shown in Fig. 21, the proposed machine has a dual-stator, single-rotor structure in which the rotor is sandwiched between the inner and outer stator. To locate the rotor PMs, a stainless-steel rotor shell is manufactured. Fig. 21 shows that 13 magnet cavities are fabricated on both the front and rear ends of the rotor shell. In order to provide sufficient mechanical strength, the outer stator is connected to the machine housing, and the inner stator is connected to a supporting shaft extended from the rear end cover. Meanwhile, the front end of the rotor support is fixed with the output shaft by bolts, and a bearing is employed to hold the output shaft on the machine housing. On the rear side, the other bearing is used to hold the rotor shell on the inner stator support.

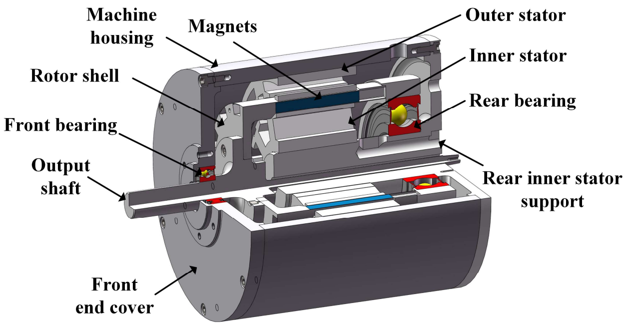

Fig.21. Subdivision of the proposed machine configuration.

The manufactured main components and their assemblies are shown in Fig. 22. The test rigs are presented in Fig. 23. A servo motor is adopted as the load machine, as shown in Fig. 23(a). Fig. 23(b) illustrates the cogging torque test rig. The stator is held rigid by a dividing head, and a balanced beam is fixed to the motor shaft to measure force. By rotating the dividing head, the variation of force at different positions can be obtained, and the corresponding torque can be calculated.

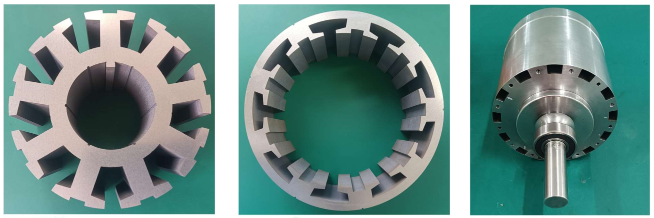

Inner stator (a) **Outer stator** (b) **Rotor** (c)

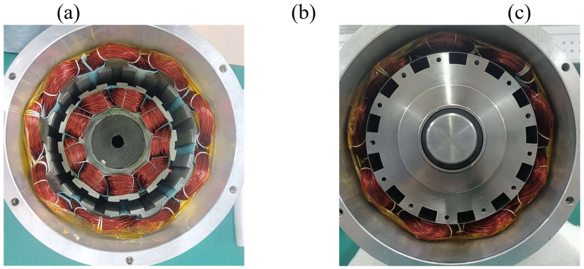

Stator assembly (d) **Prototype** (e)

Fig. 22. The prototype of the proposed DS-VPMM. (a) Inner stator. (b) Outer stator. (c) Rotor. (d) Stator assembly. (e) Prototype.

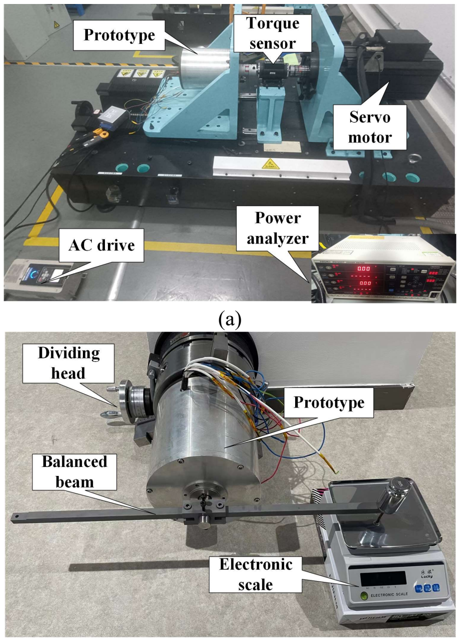

(a)

(b)

Fig. 23. The test rigs of the proposed DS-VPMM. (a) Load test rig. (b) Cogging torque test rig.

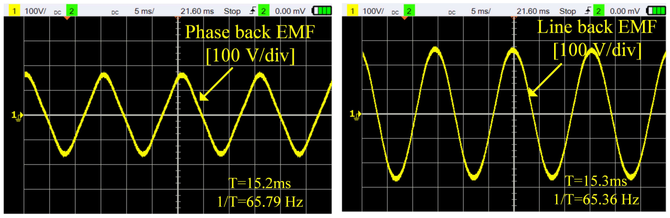

(a) (b)

Fig. 24. Measured waveforms of No-load back EMFs. (a) Phase back EMF. (b) Line back EMF.

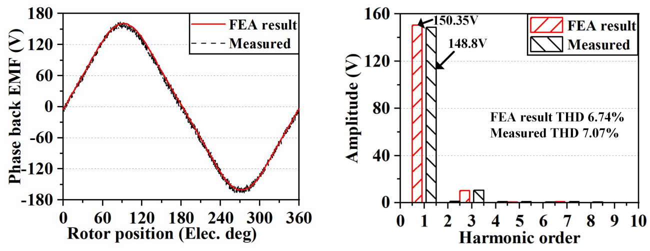

(a) (b)

Fig. 25. No-load phase back EMF. (a) Waveforms. (b) Harmonics distribution.

Fig. 24(a) and (b) depict the measured waveforms of no-load phase back EMF and line back EMF, respectively, when the proposed machine rotates at its rated speed of 300rpm. In addition, the comparisons between the simulated and measured no-load phase back EMF and line back EMF waveforms are illustrated in Fig. 25(a) and Fig. 26(a). The results demonstrate good agreement between the measured values and FEA results. Furthermore, Fig. 25(b) and Fig. 26(b) compare the total harmonic distortion (THD) of both the phase back EMF waveforms and line back EMF waveforms. It is worth noting that the THD values of the line-back EMF are lower than those of the phase-back EMF, mainly because the 3rd-order harmonic can be canceled out when measuring the line voltage in a three-phase Y connection. It is also observed that the measured THD value of the line-back EMF is slightly higher at 1.37% than the FEA result, which is at 0.43%.

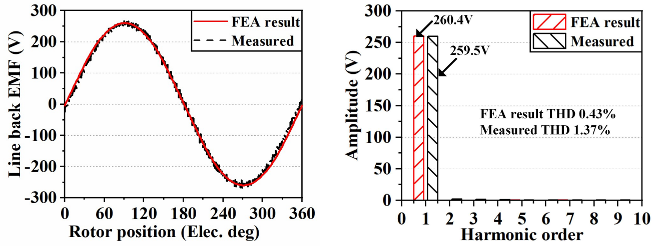

(a) (b)

Fig. 26. No-load line back EMF. (a) Waveforms. (b) Harmonics distribution.

Fig. 27 (a) shows the current waveform of phase A under the rated condition. The waveform is sinusoidal with negligible high-order harmonics, as shown in Fig. 27(b). Fig. 28(a) compares the output torque waveforms of FEA and measured results under the rated condition. Due to the inherent limitations of the test platform, the sampling time step is set as 1 second. It can be observed that both waveforms perform small fluctuations during 100 seconds, which is mainly due to the bandwidth limit of the torque sensor. The cogging torque is an important factor affecting torque ripple. To further validate the torque variation of the proposed machine, cogging torque is measured. The test result and simulation result are compared in Fig. 28(b). The measured cogging torque is 0.43Nm, which is larger than the simulation result. This deviation is mainly caused by the mechanical tolerance during the prototype manufacture.

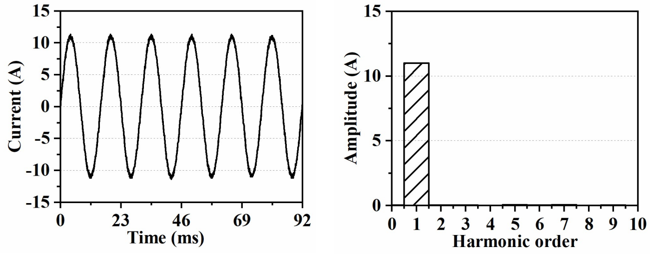

(a) (b)

Fig. 27. Meauserd phase current under the rated condition (I_{rms}=7.8A). (a) Waveform. (b) Harmonics distribution.

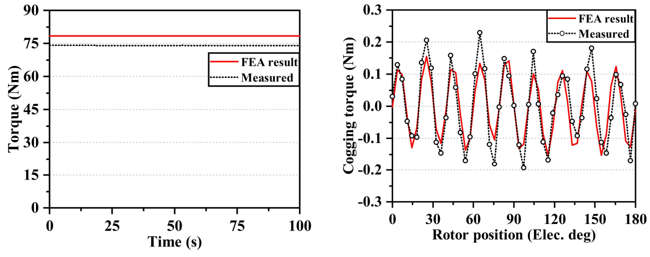

(a) (b)

Fig. 28. Torque performance. (a) Output torque under rated current. (b) Cogging torque.

In addition, the estimated torque from FEA and the measured torque against current curves are presented in Fig. 29. Although

This article has been accepted for publication in IEEE Journal of Emerging and Selected Topics in Power Electronics. This is the author's version which has not been fully edited and content may change prior to final publication. Citation information: DOI 10.1109/JESTPE.2023.3315560

a minor discrepancy can be observed between the FEA and measured values when the input current varies from 0 to 10A, the overall trends of these results are consistent.

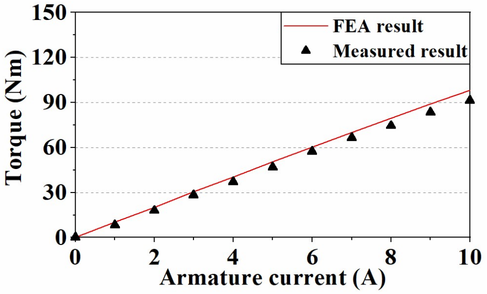

Fig.29. Comparison of FEA and measured average torque versus the phase current.

Finally, Table VI summarizes the FEA and measured results of the prototype. The output torque of the measured value is 5.53% lower than the FEA result. The measured value of synchronous inductance is also slightly lower than the FEA results. The measured power factor is 0.939, higher than the FEA predicted. These minor discrepancies are mainly due to the end-effect, manufacturing tolerance, and the performance difference between the silicon steel in simulation and manufacturing are not considered in FEA. Although there are some slight differences between the FEA and measured values, the results are generally matched well, confirming the effectiveness of the proposed DS-VPMM.

TABLE VI
PERFORMANCE COMPARISON OF SIMULATION AND MEASURED RESULTS

Items	Simulated result	Measured result
Speed (rpm)	300	
Rated current (A)	7.8	
Torque (Nm)	78.34	74.07
Synchronous inductance (mH)	18.8	16.94
Power factor	0.91	0.939

VI. CONCLUSION

In this paper, a novel DS-VPMM with a special winding arrangement is proposed. The power factor can be improved from 0.62 to 0.91 under the rated condition. By analyzing the air gap working harmonics, it is found that only odd-order space harmonics contribute to torque production. Hence, the novel design concept of reducing the non-working even-order space harmonics in armature reaction is very attractive, while the odd-order working harmonics are unaffected. The synchronous inductance is effectively reduced, and the power factor is highly improved. The FEA simulation is conducted to verify the analysis, and the electromagnetic characteristics of the proposed and conventional machines are compared. The simulation results show that in addition to the higher power factor, the proposed DS-VPMM machine also exhibits a larger average torque, a better overload capability, and a lower unbalanced force. The average torque is enhanced by 30.1%, and the unbalanced force is reduced by 76.4%. Moreover, a prototype is manufactured and tested. The experiment results well verify the analysis and simulation results.

ACKNOWLEDGMENT

This work was supported by the Research Grant Council of the Hong Kong Government under Project PolyU 152109/20E.

REFERENCES

[1] K. T. Chau, C. C. Chan, and Chunhua Liu, “Overview of permanent-magnet brushless drives for electric and hybrid electric vehicles,” *IEEE Trans. Ind. Electron.*, vol. 55, no. 6, pp. 2246–2257, Jun. 2008.
[2] L. Guo, K. Wang, and T. Wang, “Open-circuit fault diagnosis of three-phase permanent magnet machine utilizing normalized flux-producing current,” *IEEE Trans. Ind. Electron.*, DOI: 10.1109/TIE.2023.3273254.
[3] K. Wang, J. Li, S. S. Zhu and C. Liu, "Novel hybrid-pole rotors for consequent-pole PM machines without unipolar leakage flux," *IEEE Trans. Ind. Electron.*, vol. 66, no. 9, pp. 6811-6823, Sept. 2019.
[4] L. Jian, G. Xu, C. C. Mi, K. T. Chau, and C. C. Chan, “Analytical method for magnetic field calculation in a low-speed permanent-magnet harmonic machine,” *IEEE Trans. Energy Convers.*, vol. 26, no. 3, pp. 862–870, Sep. 2011.
[5] Z. Q. Zhu and Y. Liu, “Analysis of air-gap field modulation and magnetic gearing effect in fractional-slot concentrated-winding permanent-magnet synchronous machines,” *IEEE Trans. Ind. Electron.*, vol. 65, no. 5, pp. 3688-3698, May 2018.
[6] S. L. Ho, S. Niu and W. N. Fu, “Design and comparison of Vernier permanent magnet machines,” *IEEE Trans. Magn.*, vol. 47, no. 10, pp. 3280-3283, Oct. 2011.
[7] Z. S. Du and T. A. Lipo, “Design of an improved dual-stator ferrite magnet Vernier machine to replace an industrial rare-earth IPM machine,” *IEEE Trans. Energy Convers.*, vol. 34, no. 4, pp. 2062-2069, Dec. 2019.
[8] X. Zhao, S. Niu, X. Zhang and W. Fu, “A new relieving-DC-saturation hybrid excitation Vernier machine for HEV starter generator application,” *IEEE Trans. Ind. Electron.*, vol. 67, no. 8, pp. 6342-6353, Aug. 2020.
[9] Q. Lin, S. Niu, and W. N. Fu, “Design and optimization of a dual-permanent-magnet Vernier machine with a novel optimization model,” *IEEE Trans. Magn.*, vol. 56, no. 3, pp. 1–5, Mar. 2020.
[10] Y Zhang, D Li, P Yan, X Ren, et al. “A high torque density claw pole-permanent magnets vernier machine”. *IEEE Jour. Emer. Select. Topics in Pow. Elect.*, vol.10, no.2, pp: 1756-1765, April 2022.
[11] L Fang, D Li, X Ren and Qu R, “A Novel permanent magnet vernier machine with coding-shaped tooth”. *IEEE Trans. Ind. Electron.*, vol.69, no.6, pp: 6058-6068, June 2022.
[12] B. Kim and T. A. Lipo, “Operation and design principles of a PM Vernier motor,” *IEEE Trans. Ind. Appl.*, vol. 50, no. 6, pp. 3656–3663, Nov./Dec. 2014.
[13] Y. Kataoka, M. Takayama, Y. Matsushima, and Y. Anazawa, “Comparison of three magnet array-type rotors in surface permanent magnet-type Vernier motor,” *15th Int. Conf. Elect. Mach. Syst. (ICEMS)*, Oct. 2012, pp. 1–6.
[14] T. W. Ching, K. T. Chau and W. Li, “Power factor improvement of a linear Vernier permanent-magnet machine using auxiliary DC field excitation,” *IEEE Trans. Magn.*, vol. 52, no. 7, pp. 1-4, Jul. 2016.
[15] Z. Yu, W. Kong, D. Li, R. Qu and C. Gan, “Power factor analysis and maximum power factor control strategy for six-phase DC-biased Vernier reluctance machines,” *IEEE Trans. Ind. Appl.*, vol. 55, no. 5, pp. 4643-4652, Sept./Oct. 2019.
[16] D. Li, R. Qu and T. A. Lipo, “High-power-factor Vernier permanent-magnet machines,” *IEEE Trans. Ind. Appl.*, vol. 50, no. 6, pp. 3664-3674, Nov./Dec. 2014.
[17] L. Wu and R. Qu, “A novel dual-stator Vernier permanent magnet machine with improved power factor,” *IEEE Trans. Ind. Appl.*, vol. 58, no. 3, pp. 3486-3496, May/Jun. 2022.
[18] Y. Liu, H. Y. Li and Z. Q. Zhu, “A high-power factor Vernier machine with coil pitch of two slot pitches,” *IEEE Trans. Magn.*, vol. 54, no. 11, pp. 1-5, Nov. 2018.
[19] D. Li, T. Zou, R. Qu, and D. Jiang, “Analysis of fractional-slot concentrated winding PM Vernier machines with regular open-slot stators,” *IEEE Trans. Ind. Appl.*, vol. 54, no. 2, pp. 1320–1330, Mar./Apr. 2018.
[20] Y. Liu and Z. Q. Zhu, “Electromagnetic performance comparison of 18-slot/26-pole and 18-slot/10-pole fractional slot permanent magnet surface-mounted machines,” *20th Int. Conf. Elect. Mach. Syst. (ICEMS)*, 2017, pp. 1-6.

[21] S. Xie et al., "A new hybrid concentrated-winding concept with improved power factor for permanent magnet vernier machine," *IEEE Trans. Ind. Electron.*, vol. 70, no. 11, pp. 11109–11120, Nov. 2023.

[22] G. Dajaku, S. Spas, and D. Gerling, "Advanced optimization methods for fractional slot concentrated windings," *Electr Eng.*, vol. 101, no. 1, pp. 103–120, Apr. 2019.

[23] G. Dajaku, W. Xie, and D. Gerling, "Reduction of low space harmonics for the fractional slot concentrated windings using a novel stator design," *IEEE Trans. M*agn., vol. 50, no. 5, pp. 1–12, May 2014.

[24] G. J. Li, Z. Q. Zhu, W. Q. Chu, M. P. Foster and D. A. Stone, "Influence of flux gaps on electromagnetic performance of novel modular PM machines," *IEEE Trans. Energy Convers.*, vol. 29, no. 3, pp. 716-726, Sep. 2014.

[25] G. Dajaku and D. Gerling, "Eddy current loss minimization in rotor magnets of PM machines using high-efficiency 12-teeth/10-poles winding topology," *Int. Conf. Elect. Mach. Syst. (ICEMS)*, Beijing, China, Aug. 2011, pp. 1–6.

[26] L. Alberti and N. Bianchi, "Theory and design of fractional-slot multilayer windings," *IEEE Trans. Ind. Appl.*, vol. 49, no. 2, pp. 841-849, Mar./Apr. 2013.

[27] A. S. Abdel-Khalik, S. Ahmed and A. M. Massoud, "Low space harmonics cancelation in double-layer fractional slot winding using dual multiphase winding," *IEEE Trans. Magn.*, vol. 51, no. 5, pp. 1-10, May 2015.

[28] V. M. Sundaram and H. A. Toliyat, "A fractional slot concentrated winding (FSCW) configuration for outer rotor squirrel cage induction motors," *2015 IEEE International Electric Machines & Drives Conference (IEMDC),* May 2015, pp. 20-26.

[29] K. Wang, Z. Q. Zhu and G. Ombach, "Synthesis of high performance fractional-slot permanent-magnet machines with coil-pitch of two slot-pitches," *IEEE Trans. Energy Convers.*, vol. 29, no. 3, pp. 758-770, Sep. 2014.

[30] H. Y. Sun and K. Wang, "Space harmonics elimination for fractional-slot windings with two-slot coil pitch," *IEEE Access*, vol. 7, pp. 106961-106972, 2019.

[31] Y. Chen, W. Fu, and X. Weng, "A concept of general flux-modulated electric machines based on a unified theory and its application to developing a novel doubly-fed dual-stator motor," *IEEE Trans. Ind. Electron.*, vol. 64, no. 12, pp. 9914–9923, Dec. 2017.

[32] H. Yang, Z. Q. Zhu, H. Lin, H. Li and S. Lyu, "Analysis of consequent-pole flux reversal permanent magnet machine with biased flux modulation theory," *IEEE Trans. Ind. Electron.*, vol. 67, no. 3, pp. 2107-2121, Mar. 2020.